

# Deep Separable Spatiotemporal Learning for Fast Dynamic Cardiac MRI

Zi Wang, Min Xiao, Yirong Zhou, Chengyan Wang, Naiming Wu, Yi Li, Yiwen Gong, Shufu Chang, Yinyin Chen, Lihong Zhu, Jianjun Zhou, Congbo Cai, He Wang, Di Guo, Guang Yang, and Xiaobo Qu

**Abstract**—Dynamic magnetic resonance imaging (MRI) plays an indispensable role in cardiac diagnosis. To enable fast imaging, the k-space data can be undersampled but the image reconstruction poses a great challenge of high-dimensional processing. This challenge leads to necessitate extensive training data in many deep learning reconstruction methods. This work proposes a novel and efficient approach, leveraging a dimension-reduced separable learning scheme that excels even with highly limited training data. We further integrate it with spatiotemporal priors to develop a Deep Separable Spatiotemporal Learning network (DeepSSL), which unrolls an iteration process of a reconstruction model with both temporal low-rankness and spatial sparsity. Intermediate outputs are visualized to provide insights into the network’s behavior and enhance its interpretability. Extensive results on cardiac cine datasets show that the proposed DeepSSL is superior to the state-of-the-art methods visually and quantitatively, while reducing the demand for training cases by up to 75%. And its preliminary adaptability to cardiac patients has been verified through experienced radiologists’ and cardiologists’ blind reader study. Additionally, DeepSSL also benefits for achieving the downstream task of cardiac segmentation with higher accuracy and shows robustness in prospective real-time cardiac MRI.

**Index Terms**—Deep learning, magnetic resonance imaging, dynamic imaging, image reconstruction

## I. INTRODUCTION

DYNAMIC magnetic resonance imaging (MRI) is a non-invasive and radiation-free imaging modality that can simultaneously reveal spatial anatomical structures and

temporal physiological functions [1]. It plays an indispensable role in clinical applications such as cardiac cine MRI, but suffers from the prolonged data acquisition. Accelerated imaging facilitates the achievement of high spatiotemporal resolution, improvement of patient comfort, and reduction of motion-induced artifacts [2]. For dynamic MRI acceleration, parallel imaging [3, 4] and sparse sampling [2, 5] have been widely used to provide k-t (i.e., k-space and temporal) undersampling with a high acceleration factor (AF).

Over the past two decades, to reconstruct images from undersampled data, many model-based methods have been established by exploring different signal priors to obtain promising results. Among them, sparse and low-rank priors attract the most attentions. Specifically, sparse priors are utilized for spatiotemporal data regularization in some transform domains (e.g., temporal Fourier and/or wavelet transforms [2, 6-10]). Low-rank methods commonly involve the partial separability of a Casorati matrix [5, 11] and the structured low-rankness of temporal correlations [12-14]. Moreover, based on their complementarity, some methods such as low-rank and sparse (L&S) [11, 15] and low-rank plus sparse (L+S) [16] have also emerged that combine two priors. Their excellent reconstruction performance prompts us for further development.

In recent years, deep learning has emerged as a powerful tool in dynamic MRI, providing high-quality images and ultra-fast reconstruction speed [17-20]. Unlike end-to-end deep networks directly learn the mapping for reconstruction [21, 22], many unrolled deep networks stand out by merging the advantages of

This work was supported in part by the National Natural Science Foundation of China under grants 62331021, 62122064, and 62371410, Natural Science Foundation of Fujian Province of China under grants 2023J02005, 2021J011184, and 2022J011425, President Fund of Xiamen University under grant 20720220063, UKRI Future Leaders Fellowship under grant MR/V023799/1, Xiamen University Nanqiang Outstanding Talents Program, and China Scholarship Council under grant 202306310177.

Zi Wang, Yirong Zhou, Congbo Cai, and Xiaobo Qu\* are with the Department of Electronic Science, Intelligent Medical Imaging R&D Center, Fujian Provincial Key Laboratory of Plasma and Magnetic Resonance, National Institute for Data Science in Health and Medicine, Xiamen University, China (\*Corresponding author, email: quxiaobo@xmu.edu.cn).

Min Xiao is with the Institute of Artificial Intelligence, Xiamen University, China.

Chengyan Wang and He Wang are with the Human Phenome Institute, Fudan University, China.

Naiming Wu and Yi Li are with the Department of Imaging, Xiamen Cardiovascular Hospital of Xiamen University, School of Medicine, Xiamen University, China.

Yiwen Gong is with the Department of Cardiovascular Medicine, Heart Failure Center, Ruijin Hospital Lu Wan Branch, Shanghai Jiaotong University School of Medicine, China.

Shufu Chang is with the Shanghai Institute of Cardiovascular Diseases, Zhongshan Hospital, Fudan University, China.

Yinyin Chen is with the Department of Radiology, Zhongshan Hospital, Fudan University, Department of Medical Imaging, Shanghai Medical School, Fudan University and Shanghai Institute of Medical Imaging, China.

Lihong Zhu and Jianjun Zhou are with the Department of Radiology, Zhongshan Hospital, Fudan University (Xiamen Branch), Fujian Province Key Clinical Specialty Construction Project (Medical Imaging Department), Xiamen Key Laboratory of Clinical Transformation of Imaging Big Data and Artificial Intelligence, China.

Di Guo is with the School of Computer and Information Engineering, Xiamen University of Technology, China.

Guang Yang is with the Department of Bioengineering and Imperial-X, Imperial College London, United Kingdom.

Zi Wang is also with the Department of Bioengineering, Imperial College London, United Kingdom.

model-based and deep learning methods mentioned above [23-26]. These methods often unroll the iterative solving process of conventional models to deep networks and effectively utilize the unique MRI physical information (e.g., data consistency and coil sensitivity encoding [23, 24]) and/or explore the signal priors (e.g., sparsity and low-rankness [25, 26]). In addition to presenting promising results, part of them also attempt to provide a certain interpretability [20].

Dynamic cardiac MRI reconstruction is a natural high-dimensional problem with high computational complexity. Up to now, most existing deep learning methods [22-26] still try to confront this complex problems directly and require numerous training data to obtain satisfactory results. However, dynamic cardiac MRI data collection is often time-consuming and highly susceptible to the cardiac/respiratory-induced motion [27, 28], leading to the scarcity of available training data. Therefore, developing a new method that can effectively train an image reconstruction network with limited training data is expected.

In this work, we a new separable learning scheme for 2D dynamic cardiac MRI reconstruction. Through reducing the problem dimensionality from 3D to 2D, it alleviates the high dependence of deep networks on the number of training datasets. Fig. 1 illustrates an example that our separable learning is far superior to direct learning methods [24, 25] when training cases are highly limited (e.g., only 5 cases from *in vivo* dataset).

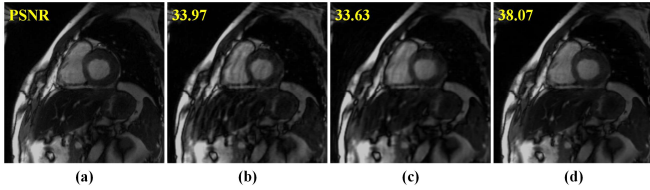


Fig. 1. A cardiac cine reconstruction example using only 5 cases from *in vivo* dataset for network training. (a) Fully sampled image. (b)-(c) are reconstructed images of two state-of-the-art direct learning methods DL-ESPIRiT [24] and SLR-Net [25], respectively. (d) is the reconstructed image of our separable learning method. Note: The k-t random undersampling pattern with AF=6 is used. PSNR(dB) is listed for each reconstruction.

This idea is primarily inspired by the recent success of 1D learning on static MRI reconstruction [29, 30]. Specifically, for the Cartesian 2D dynamic MRI, the frequency encoding (FE) direction is always fully sampled, while the imaging acceleration happens in the phase encoding-temporal (PE-t) space by randomly skipping the PE for each temporal frame (Figs. 2(a)-(c)). Then, by taking the 1D inverse Fourier transform (IFT) along the FE, the 3D k-t data can be separate into many 2D k-t data. It is easy to find that all 2D k-t data actually have the same undersampling scenario (Fig. 2(d)), so we can train a deep network on 2D samples instead of the whole 3D ones, to alleviate the computational challenges. In addition to reducing the scale of the reconstruction problem from 3D to 2D, it also leads to the significant data enlargement with a factor equal to the dimension of FE.

Moreover, we integrate the dimension-reduced separable learning scheme with spatiotemporal priors to develop a Deep Separable Spatiotemporal Learning network (DeepSSL). It formulates both temporal low-rank and spatial sparse priors as

regularized terms in an optimization model and unroll its iteration process into a deep network.

Our main contributions are summarized as follows:

1) The proposed method significantly alleviates the training and generalization challenges of deep learning in dynamic MRI through efficient dimension-reduced separable learning and spatiotemporal modeling.

2) The designed network unrolls the iteration process of a reconstruction model, which simultaneously explores the temporal low-rankness and image sparsity. We also explain our network by visualizing the intermediate results.

3) Extensive results show that, for both healthy cases and patients, the proposed DeepSSL provides superior performance under objective criteria and blind reader study. Besides, it can further benefit the downstream task of cardiac segmentation and achieve prospective real-time cardiac MRI reconstruction.

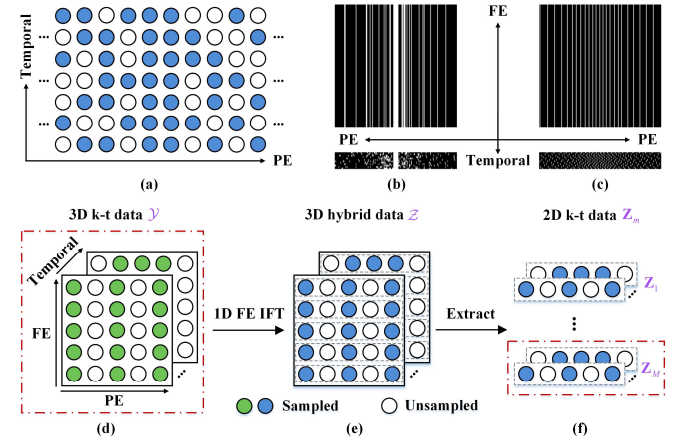


Fig. 2. Graphical illustration of the k-t undersampling and the process of reducing the scale of the reconstruction problem from 3D to 2D. (a) is the undersampling in the PE-t space. (b) is the k-t random undersampling pattern. (c) is the k-t variable density incoherent spatiotemporal acquisition (VISTA) pattern [31]. The regions marked by the red rectangle represent one of the (d) 3D and (f) 2D reconstruction, respectively. Note: The proposed method can handle multi-coil data but the coil dimension is omitted here for plot simplification.

## II. PROPOSED METHOD

In this section, we first formulate our basic problem on dynamic MRI and introduce the proposed dimension-reduced separable learning scheme. Then, a corresponding 2D k-t reconstruction model is presented, which simultaneously utilizes temporal low-rankness [12, 13] and spatial sparsity [2, 32]. Finally, the iteration process of a conventional reconstruction algorithm is unrolled to a deep network and its implementation details are introduced.

### A. Problem Formulation

For the k-t undersampling in Cartesian 2D dynamic MRI, the 3D k-t reconstruction can be split into several 2D k-t reconstructions as follows (Figs. 2(d)-(f)):

Consider the multi-coil 3D k-t data  $\mathcal{Y} \in \mathbb{C}^{M \times N \times T}$  with non-acquired positions zero-filled and  $\mathcal{U}$  is an operator that performs undersampling.  $M, N, T, J$  represent the dimension of the FE, PE, temporal frame, and coil, respectively.

Taking the 1D FE IFT  $\mathcal{F}_{FE}^*$  of  $\mathcal{Y}$ , we can obtain the 3D hybrid data  $\mathcal{Z} \in \mathbb{C}^{M \times N \times T}$  (Fig. 2(e)):

$$\mathcal{Z} = \mathcal{F}_{FE}^* \mathcal{Y} = \mathcal{F}_{FE}^* \mathcal{U} \mathcal{F}_{2D} \mathcal{S} \mathcal{X} = \mathcal{U} \mathcal{F}_{PE} \mathcal{S} \mathcal{X} = \mathcal{A} \mathcal{X}, \quad (1)$$

where  $\mathcal{X} \in \mathbb{C}^{M \times N \times T}$  is the 3D spatiotemporal image,  $\mathcal{S}$  is the coil sensitivity encoding operator.  $\mathcal{F}_{2D}, \mathcal{F}_{PE}$  represent the 2D spatial FT and 1D PE FT, respectively. Here, for simplicity, we define the forward encoding operator as  $\mathcal{A} = \mathcal{U} \mathcal{F}_{PE} \mathcal{S}$ .

Given the 1D IFT decoupling, the  $m^{\text{th}}$  row data  $\mathbf{Z}_m \in \mathbb{C}^{N \times T}$  of  $\mathcal{Z}$  can be treated as an independent 2D k-t signal (Fig. 2(f)). Accordingly, the  $m^{\text{th}}$  row data  $\mathbf{X}_m \in \mathbb{C}^{N \times T}$  of  $\mathcal{X}$  is treated independently, since  $\mathcal{A}$  can be performed on each 2D spatiotemporal image directly. After reconstructing all  $\mathbf{X}_m$ , we can combine them sequentially along the FE to yield the reconstructed 3D spatiotemporal image  $\hat{\mathcal{X}} \in \mathbb{C}^{M \times N \times T}$ .

### B. Dimension-Reduced Separable Learning Scheme

There are two core steps for our proposed dimension-reduced separable learning scheme: Build paired 2D k-t training datasets and train the corresponding deep network.

Fig. 3 presents the overall concept of our separable learning scheme. In step one, for a fully sampled 3D k-t data (Fig. 3(a)), we undersample it and take the 1D FE IFT to obtain the undersampled 3D hybrid data (Fig. 3(c)). Then, we extract the same row of the undersampled 3D hybrid data and fully sampled 3D spatiotemporal image as a paired 2D training sample. After that, the paired 2D training dataset is built for network training, where the undersampled 2D k-t data is input (Fig. 3(d)) and the fully sampled 2D spatiotemporal image is label (Fig. 3(f)).

Then, in step two, we train the deep network by minimizing the loss function between reconstructed 2D spatiotemporal images (Fig. 3(e)) and labels. Eventually, the well-trained network can be applied to dynamic MRI reconstructions.

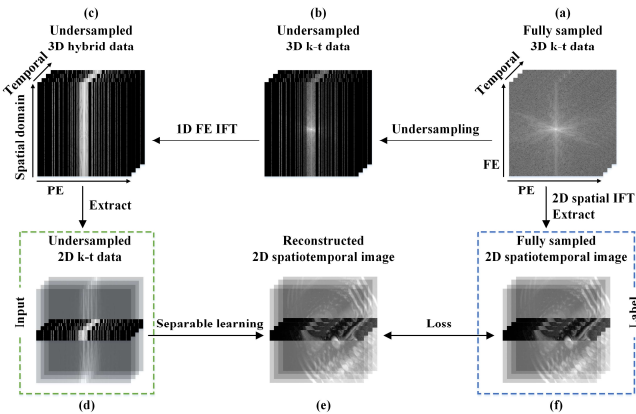


Fig. 3. Flowchart of our dimension-reduced separable learning. Note: The regions marked by the (d) green and (f) blue rectangle represent the network input and label, respectively. The coil dimension is omitted for simplification.

### C. Reconstruction Model

We build a 2D k-t reconstruction model with spatiotemporal priors. Specifically, it simultaneously utilizes the low-rankness of temporal inter-frame correlations [12, 13] and spatial sparsity

in some transform domains [2, 32].

Here, the low-rank property is implicitly characterized by the null space filterbank  $\mathbf{Q}$  of all temporal signals  $\mathcal{E}_n \mathbf{X}_m \in \mathbb{C}^T$  [12], while the sparsity of all spatial signals  $\mathcal{V}_t \mathbf{X}_m \in \mathbb{C}^N$  in some transform domains [32] is added for further improvement. The  $\mathcal{E}_n$  and  $\mathcal{V}_t$  denote operators that extract  $n^{\text{th}}$  vector on the first dimension and  $t^{\text{th}}$  vector on the second dimension from  $\mathbf{X}_m$ .

Thus, the 2D k-t reconstruction model with these two priors can be formulated as

$$\min_{\mathbf{X}_m} \frac{1}{2} \|\mathbf{Z}_m - \mathcal{A} \mathbf{X}_m\|_2^2 + \lambda_1 \sum_{n=1}^N \|\mathcal{P}(\mathbf{Q}) \mathcal{E}_n \mathbf{X}_m\|_F^2 + \lambda_2 \sum_{t=1}^T \|\mathcal{D} \mathcal{V}_t \mathbf{X}_m\|_1, \quad (2)$$

where  $\mathcal{A} = \mathcal{U} \mathcal{F}_{PE} \mathcal{S}$  is the forward encoding operator.  $\mathcal{P}(\mathbf{Q})$  is the vertically cascaded Toeplitz matrix (See [29] for detailed derivations), and  $\mathcal{P}(\mathbf{Q}) \mathcal{E}_n \mathbf{X}_m$  represents the linear convolution between  $\mathbf{Q}$  and  $\mathcal{E}_n \mathbf{X}_m$ .  $\mathcal{D}$  is the sparse transform, such as tight frames [33, 34],  $\lambda_1$  and  $\lambda_2$  are regularization parameters for the temporal low-rankness term and spatial sparsity term, respectively.

To solve (2), the variable-splitting algorithm [35] is chosen to decouple the data consistency term and regularization terms. By introducing auxiliary variables  $\mathbf{b}_{m,n} = \mathcal{E}_n \mathbf{X}_m$  and  $\mathbf{d}_{m,t} = \mathcal{V}_t \mathbf{X}_m$ , (2) can be solved by alternating three sub-problems and the  $k^{\text{th}}$  iteration is

$$\mathbf{b}_{m,n}^{(k)} = \arg \min_{\mathbf{b}_{m,n}} \lambda_1 \|\mathcal{P}(\mathbf{Q}) \mathbf{b}_{m,n}\|_F^2 + \frac{\mu_1}{2} \|\mathbf{b}_{m,n} - \mathcal{E}_n \mathbf{X}_m^{(k-1)}\|_2^2, \quad (3)$$

$$\mathbf{d}_{m,t}^{(k)} = \arg \min_{\mathbf{d}_{m,t}} \lambda_2 \|\mathcal{D} \mathbf{d}_{m,t}\|_1 + \frac{\mu_2}{2} \|\mathbf{d}_{m,t} - \mathcal{V}_t \mathbf{X}_m^{(k-1)}\|_2^2, \quad (4)$$

$$\mathbf{X}_m^{(k)} = \arg \min_{\mathbf{X}_m} \|\mathbf{Z}_m - \mathcal{A} \mathbf{X}_m\|_2^2 + \mu_1 \sum_{n=1}^N \|\mathbf{b}_{m,n}^{(k)} - \mathcal{E}_n \mathbf{X}_m\|_2^2 + \mu_2 \sum_{t=1}^T \|\mathbf{d}_{m,t}^{(k)} - \mathcal{V}_t \mathbf{X}_m\|_2^2. \quad (5)$$

Finally, the solutions of (3)-(5) constitutes the following iteration process of our reconstruction model:

$$\begin{cases} \mathbf{b}_{m,n}^{(k)} = \mathcal{E}_n \mathbf{X}_m^{(k-1)} - \frac{2\lambda_1}{\mu_1} (\mathcal{P}(\mathbf{Q}))^H \mathcal{P}(\mathbf{Q}) \mathcal{E}_n \mathbf{X}_m^{(k-1)} \\ \mathbf{d}_{m,t}^{(k)} = \mathcal{D}^* [\text{soft}(\mathcal{D} \mathcal{V}_t \mathbf{X}_m^{(k-1)}; \frac{\lambda_2}{\mu_2})] \\ \mathbf{X}_m^{(k)} = (\mathcal{A}^* \mathcal{A} + \mu_1 \sum_{n=1}^N \mathcal{E}_n^* \mathcal{E}_n + \mu_2 \sum_{t=1}^T \mathcal{V}_t^* \mathcal{V}_t)^{-1} (\mathcal{A}^* \mathbf{Z}_m + \mu_1 \mathbf{B}_m^{(k)} + \mu_2 \mathbf{D}_m^{(k)}) \end{cases}, \quad (6)$$

where  $\mu_1$  and  $\mu_2$  are penalty parameters, the superscript  $*$  is the adjoint operation, and  $\text{soft}(x; \rho) = \max\{|x| - \rho, 0\} \cdot x / |x|$  is the element-wise soft-thresholding. For simplicity, we define

$$\mathbf{B}_m = \sum_{n=1}^N \mathcal{E}_n^* \mathbf{b}_{m,n} \quad \text{and} \quad \mathbf{D}_m = \sum_{t=1}^T \mathcal{V}_t^* \mathbf{d}_{m,t}.$$

Conventional reconstruction algorithm iteratively updates each variable in (6) until convergence. Thus, the whole process is always time-consuming, while all regularization constraints and parameters are cumbersome and manually determined [36].

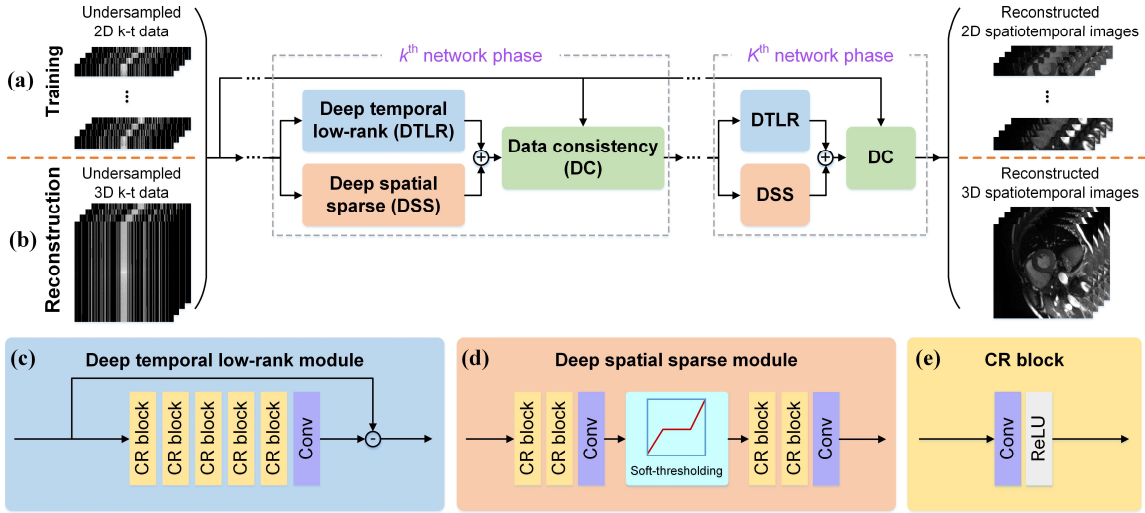


Fig. 4. The proposed DeepSSL for dynamic MRI reconstruction. This is the recursive network architecture in (a) training and (b) reconstruction stages. With the increase of the network phase, artifacts are gradually removed, and a high-quality reconstructed image can be obtained finally (See Section. D). (c)-(d) are the detailed structures of network modules. Note: “Conv” is the convolution. “CR” is the convolution followed by a ReLU activation.

#### D. Deep Separable Spatiotemporal Learning Network

In this work, we propose a Deep Separable Spatiotemporal Learning network (DeepSSL) by unrolling the iteration process in (6) to a deep network. As shown in Fig. 4, three network modules are elaborately designed, which correspond to three sub-problems in (6). They are name as deep temporal low-rank module, deep spatial sparse module, and data consistency module. Note that, all regularization and penalty parameters, sparse transform  $\mathcal{D}$ , and filterbank  $\mathbf{Q}$  become learnable.

Specifically, our deep temporal low-rank module performs 1D convolution on each temporal signal for null space projection, then eliminate it to remove the artifacts and noise of the temporal domain. Meanwhile, in deep spatial sparse module, 1D convolution is performed on each spatial signal to achieve anti-aliasing. After repeating three modules several times, the final 2D spatiotemporal image is reconstructed. The detailed description of three modules are as follows.

##### 1) Deep Temporal Low-Rank Module

Fig. 4(c) shows the deep temporal low-rank module that corresponds to the first sub-equation of (6).  $(\mathcal{P}(\mathbf{Q}))^H \mathcal{P}(\mathbf{Q}) \mathcal{E}_n \mathbf{X}_m$  stands for projecting  $\mathcal{E}_n \mathbf{X}_m$  to a null space to kill all meaningful signals while preserve artifacts and noise. This linear null space projection is a filterbank determined by  $\mathbf{Q}$  [12, 13].

In this work, we directly use the multi-layer convolutional network to replace  $(\mathcal{P}(\mathbf{Q}))^H \mathcal{P}(\mathbf{Q})$  to achieve nonlinear null space projection, as network has strong representation ability [29, 37]. Then, we subtract these artifacts and noise from input  $\mathcal{E}_n \mathbf{X}_m$  for temporal de-aliasing, which is similar to a form of residual learning [38]. Thus, the deep temporal low-rank module is designed as

$$\mathbf{b}_{m,n}^{(k)} = \mathcal{E}_n \mathbf{X}_m^{(k-1)} - \mathcal{N}_1(\mathcal{E}_n \mathbf{X}_m^{(k-1)}), \quad (7)$$

where  $\mathcal{N}_1$  is a multi-layer convolutional network. When  $k = 1$ ,

the initialized input  $\mathbf{X}_m^{(0)} = \mathcal{A}^* \mathbf{Z}_m$  is the zero-filled data that has strong artifacts.

Fig. 5 visualizes the nonlinear null space projection achieved by our designed network  $\mathcal{N}_1$  and the output of this module. These observations imply that, it can successfully realize proper null space estimation to primarily preserve artifact-related signals. Moreover, with the increase of network phases, the output of  $\mathcal{N}_1$  gradually approaches zero, indicating that artifacts are gradually removed and a high-quality image is yielded finally. This visualization provides a good interpretation to understand the network behavior.

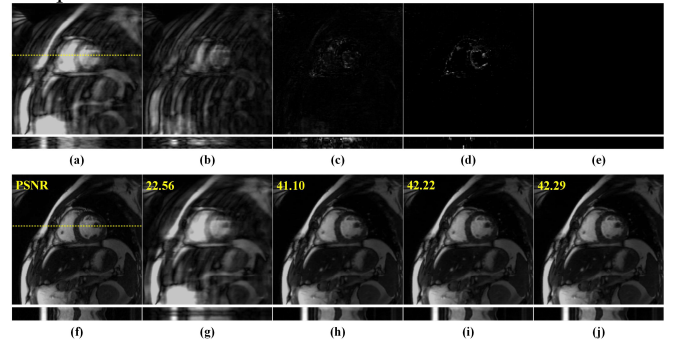


Fig. 5. The null space projections and reconstructed images of the deep temporal low-rank module at representative network phase. (a) is the zero-filled image. (b)-(e) are the null space projections at 1<sup>st</sup>, 5<sup>th</sup>, 9<sup>th</sup>, 10<sup>th</sup> (final) network phase, respectively. (f) is the fully sampled image. (g)-(j) are reconstructed images at 1<sup>st</sup>, 5<sup>th</sup>, 9<sup>th</sup>, 10<sup>th</sup> (final) network phase, respectively. Note: The k-t random undersampling pattern with AF=6 is used. The 2D spatiotemporal images are given for each reconstruction and their corresponding extracted positions are marked by the yellow dotted lines. PSNR(dB) is listed for each reconstruction.

##### 2) Deep Spatial Sparse Module

Fig. 4(d) shows the deep spatial sparse module that corresponds to the second sub-equation of (6). Here, replacing the manual-craft transform  $\mathcal{D}$  and threshold  $\lambda_2/\mu_2$ , we utilize the widely used deep thresholding network [29, 39, 40], to learn

a more general sparse transform from training datasets. Thus, the deep spatial sparse module is designed as

$$\mathbf{d}_{m,t}^{(k)} = \mathcal{N}_3[\text{soft}(\mathcal{N}_2(\mathcal{V}_r \mathbf{X}_m^{(k-1)}); \theta^{(k)})], \quad (8)$$

where  $\theta^{(k)}$  is the learnable threshold initialized to 0.001 and it is allowed to vary at each network phase. Note that, two multi-layer convolutional networks  $\mathcal{N}_2$  and  $\mathcal{N}_3$  on both sides of the soft-thresholding operator are relaxed without any invertible constraint.

### 3) Data Consistency Module

In this module, each final output is forced to maintain the data consistency to the measured data, which corresponds to the third sub-equation of (6). Here, the data consistency module is denoted more intuitively as

$$(\mathcal{F}_{PE} \mathbf{S} \mathbf{X}_m^{(k)})_p = \begin{cases} \left( \frac{\mu_1^{(k)} \mathcal{F}_{PE} \mathbf{S} \mathbf{B}_m^{(k)} + \mu_2^{(k)} \mathcal{F}_{PE} \mathbf{S} \mathbf{D}_m^{(k)}}{\mu_1^{(k)} + \mu_2^{(k)}} \right)_p, & p \notin \Omega \\ \left( \frac{\mathbf{Z}_m + \mu_1^{(k)} \mathcal{F}_{PE} \mathbf{S} \mathbf{B}_m^{(k)} + \mu_2^{(k)} \mathcal{F}_{PE} \mathbf{S} \mathbf{D}_m^{(k)}}{1 + \mu_1^{(k)} + \mu_2^{(k)}} \right)_p, & p \in \Omega \end{cases}, \quad (9)$$

where  $p$  is the index and  $\Omega$  is the set of the measured positions in k-t data.  $\mu_1^{(k)}$  and  $\mu_2^{(k)}$  set as learnable parameters initialized to 1 and are changed at each network phase. This module implies that, at the measured positions, the data points should maintain a trade-off with  $\mathbf{Z}_m$ , while the update of the unmeasured data points depends entirely on the reconstruction results of other two network modules.

### E. Implementation Details

The proposed DeepSSL is an unrolled recursive network and we empirically choose  $K=10$  as the overall number of network phase, due to a trade-off between reconstruction performance and time consumption. At each network phase,  $\mathcal{N}_1$ ,  $\mathcal{N}_2$ , and  $\mathcal{N}_3$  consist of 6, 3, and 3 convolutional layers, respectively. Each convolution layer contains 48 1D convolution filters of size 3, followed by a ReLU as activation function. Note that, the last convolution layer of each module has only 2 filters, corresponding to two channels of real and imaginary parts of data.

In the training stage, our DeepSSL is trained for 50 epochs with the Adam optimizer [41]. Its initial learning rate is set to 0.001 with an exponential decay of 0.99, while the batch size is 64. The loss function is defined as:

$$\mathcal{L}(\Theta) = \frac{1}{KC} \sum_{k=1}^K \sum_{c=1}^C \left\| \mathbf{X}_m^{\text{ref},c} - \mathbf{X}_m^{(k),c} \right\|_2^2, \quad (10)$$

where  $C$  is the number of training samples, and  $\mathbf{X}_m^{\text{ref},c}$  is the label of the  $c^{\text{th}}$  training sample. DeepSSL was implemented on a server equipped with dual Intel Xeon Silver 4210 CPUs, 256 GB RAM, and the Nvidia Tesla T4 GPU (16 GB memory) in PyTorch 1.10. The typical training took about 50 hours.

In the reconstruction stage, for given undersampled 3D k-t data, we can reconstruct them through the trained DeepSSL. As shown in Fig. 4(b), the 1D FE IFT is first performed on the undersampled k-space to obtain  $\mathcal{Z} = \mathcal{F}_{FE}^* \mathcal{Y}$ , all rows of  $\mathcal{Z}$  form a batch that is then reconstructed in parallel and stitched back

together to yield the final 3D spatiotemporal image  $\hat{\mathcal{X}}$ .

## III. EXPERIMENTAL RESULTS

### A. Datasets

Two 2D cardiac cine datasets were mainly used in this paper: A dataset of healthy cases from a public CMRxRecon dataset [28] and an in-house patient dataset from our own collection. Their study protocol was Institutional Review Board approved and informed consent was obtained from volunteers before examination. The detailed acquisitions are provided below.

#### 1) Dataset of Healthy Cases

The dataset of healthy cases was acquired using a segmented TrueFISP sequence with breath-hold at a 3T MRI scanner (Siemens MAGNETOM Vida) [28]. The cardiac cycle was segmented into 12~25 phases with a temporal resolution 50 ms according to the heart rate. Other scan parameters: Spatial resolution  $2.0 \times 2.0 \text{ mm}^2$  and slice thickness 8.0 mm. The collected images include a short-axis (SAX) view, and three long-axis (LAX) views including two/three/four-chamber (2CH/3CH/4CH) views.

There are 120 cases and each case has 10 SAX slices of size  $192 \times 192$  with 12 temporal frames, and 3 LAX slices (a single slice was acquired for each 2CH/3CH/4CH view) of  $192 \times 192$  with 12 temporal frames. Here, 100 cases were used for training, 10 for validation, and the remaining 10 for test.

#### 2) Datasets of Patients

A patient dataset with hypertrophic cardiomyopathy was acquired using a segmented TrueFISP sequence with breath-hold at a 3T MRI scanner (Siemens MAGNETOM Vida). The cardiac cycle was segmented into 12~25 phases with a temporal resolution 50 ms according to the heart rate. Other scan parameters: TR/TE=3.6/1.6 ms, spatial resolution  $1.5 \times 1.5 \text{ mm}^2$ , and slice thickness 8.0 mm. The collected images include a SAX view, and three LAX views including 2CH/3CH/4CH views.

There are 5 cases and each case has 10 SAX slices of size  $246 \times 246$  with 12 temporal frames, and 3 LAX slices (a single slice was acquired for each 2CH/3CH/4CH view) of size  $224 \times 204$  with 12 temporal frames. All 5 cases were used for test.

All datasets were fully sampled k-space, and they were first retrospectively undersampled, then used for training and test. The number of coils is 10 in all two datasets. Coil sensitivity maps were pre-estimated using ESPIRiT [42].

### B. Compared Methods and Evaluation Criteria

For comparative study, a conventional method with low-rank and sparse priors L+S [16] was used as the reconstruction baseline. We also compared the proposed DeepSSL with three state-of-the-art unrolled deep learning methods including DCCNN [23], DL-ESPIRiT [24], and SLR-Net [25]. The training schemes of them are direct learning with 3D k-t data, which is different to our proposed separable learning with 2D k-t data. DCCNN introduce the data consistency in the 3D convolutional network, while DL-ESPIRiT further utilizes the 2D spatial convolution and 1D temporal convolution. SLR-Net

is a deep sparse and low-rank network with the 3D convolution and singular value decomposition. All deep learning methods were executed according to the typical setting mentioned by the authors.

Notably, by virtue of our separable learning and 1D convolution, the proposed DeepSSL is memory-efficient. It has few network parameters (564520), about 65% of DCCNN, 61% of DL-ESPIRiT, and 42% of SLR-Net.

All methods were implemented on a server equipped with dual Intel Xeon Silver 4210 CPUs, 256 GB RAM, and the Nvidia Tesla T4 GPU (16 GB memory). The typical 3D k-t data reconstruction times per slice: L+S (38.78 seconds), DCCNN (1.18 s), DL-ESPIRiT (1.09 s), SLR-Net (2.08 s), and DeepSSL (1.43 s).

To quantitatively evaluate the image reconstruction performance, we utilized three objective evaluation criteria, including the relative  $l_2$  norm error (RLNE) [43], peak signal-to-noise ratio (PSNR), and structural similarity index (SSIM) [44]. A lower RLNE, higher PSNR, and higher SSIM indicate the lower reconstruction error, less image distortions, and better details preservation in reconstructions, respectively.

### C. Ablation Study

To evaluate the contribution of deep spatial sparse module and deep temporal low-rank module to reconstructions, we compared the proposed DeepSSL with its two variants that only impose spatial or temporal priors, named as Spatial-only and Temporal-only, respectively.

Fig. 6 shows that Spatial-only network removes most spatial artifacts but remains strong temporal artifacts, while Temporal-only network captures the dynamic information more precisely and also recovers most spatial structure. The proposed DeepSSL with spatiotemporal priors outperforms other two variants both visually and quantitatively.

These results demonstrate that the key point of dynamic MRI reconstruction is to utilize the temporal prior, while the spatial prior serves as the complementary information for further performance improvement.

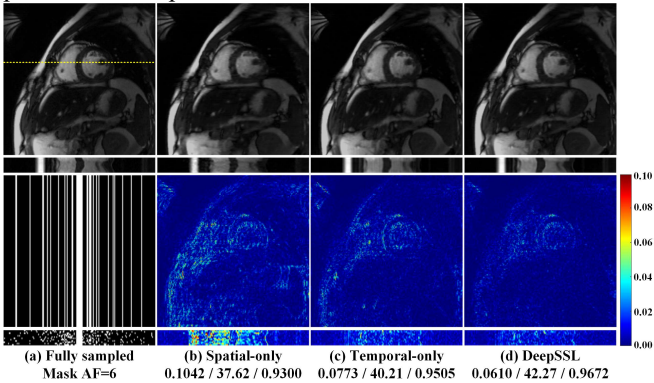


Fig. 6. Ablation study. (a) is the fully sampled image and the k-t random undersampling pattern with AF=6. (b)-(d) are reconstructed images and the corresponding error maps. Note: The 2D spatiotemporal images are given for each reconstruction and their corresponding extracted position is marked by the yellow dotted line. RLNE/PSNR(dB)/SSIM are listed for each reconstruction.

### D. Reconstruction under Varied Number of Training Cases

Here, we trained networks on a cardiac cine dataset of varied number of training cases  $N_{TC}$ , to compare the reconstruction performance of our separable learning with other state-of-the-art direct learning methods.

Fig. 7(a)-(c) show that our separable learning DeepSSL consistently outperforms other direct learning networks in terms of RLNE, PSNR, and SSIM. Even with a highly limited number of training cases ( $N_{TC} \leq 10$ ), DeepSSL already provides far superior reconstructions than the baseline L+S. In contrast, direct learning DCCNN, DL-ESPIRiT, and SLR-Net start to surpass the baseline L+S when  $N_{TC} \geq 25$ . With the increase of training cases, all methods gradually yield improvement. Finally, when a relatively large number of cases is used for training ( $N_{TC} = 100$ ), SLR-Net achieves results comparable to our DeepSSL in terms of SSIM. The similar phenomena can also be found in the reconstruction of the LAX view (Figs. 7(d)-(f)). Notably, we observed that the proposed DeepSSL can maintain the similar performance to state-of-the-art methods, while reducing the demand for training cases by up to 75% (from 100 to 25 cases).

Representative reconstructions using 100 training cases are shown in Fig. 8. L+S, DCCNN, and DL-ESPIRiT yield results exhibiting obvious spatial and temporal artifacts. SLR-Net is much better but still appear inaccurate edge brightness and cardiac details loss. The proposed DeepSSL outperforms other state-of-the-art methods in terms of three evaluation criteria, indicating the good ability of artifacts suppression and details preservation.

These results imply that, even with highly limited training data, the proposed method can work efficiently and provide state-of-the-art reconstructions of different cardiac views.

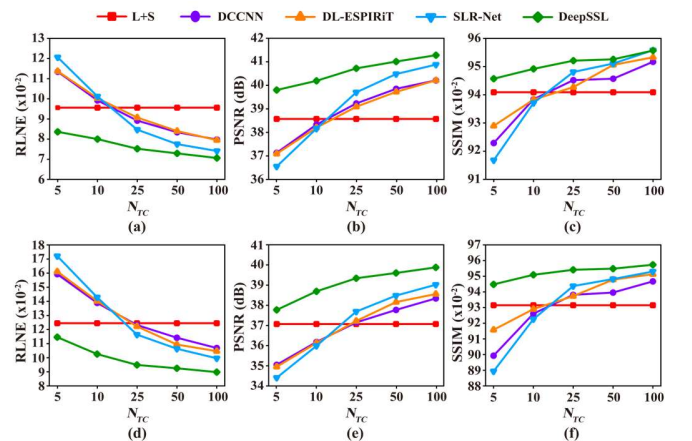


Fig. 7. Quantitative comparison of reconstructions using different number of training cases  $N_{TC}$  of a cardiac cine dataset. (a)-(c) are the mean of RLNE, PSNR, SSIM of the reconstructions of the SAX view, respectively. (d)-(f) are the mean of RLNE, PSNR, SSIM of the reconstructions of the LAX view, respectively. Note: The k-t random undersampling pattern with AF=6 is used. The means are computed over all test data.

### E. Adaptability to Patients and Reader Study

Considering that patient data often differs from healthy data, we further examined the adaptability of our method to patients,

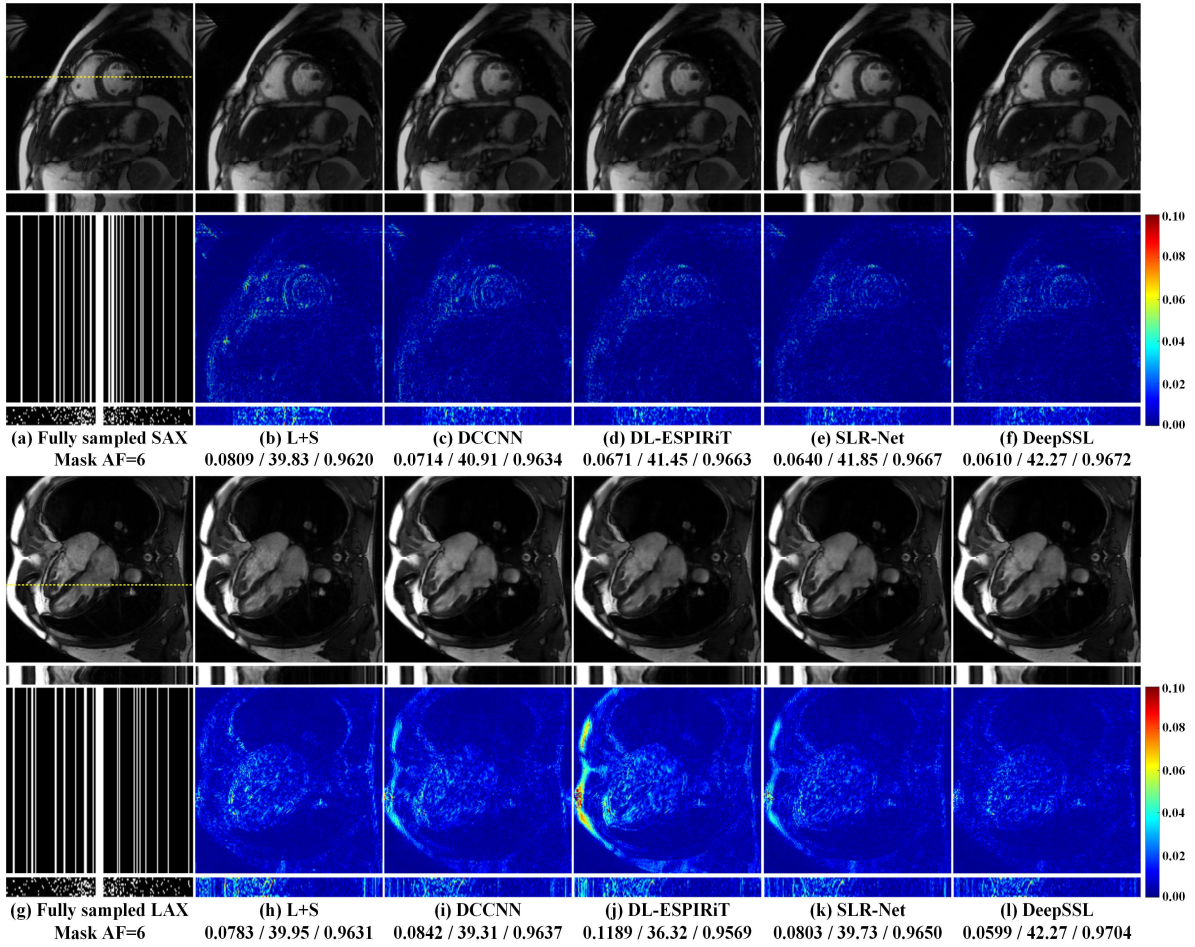


Fig. 8. Reconstruction results of a cardiac cine dataset of SAX and LAX views using different methods. (a) (or (g)) is the fully sampled image and the k-t random undersampling pattern with AF=6. (b)-(f) (or (h)-(l)) are reconstructed images and the corresponding error maps. Note: The training cases is 100. The 2D spatiotemporal images are given for each reconstruction and their corresponding extracted position is marked by the yellow dotted line. RLNE/PSNR/SSIM are listed for each reconstruction.

which is essential in clinical diagnosis. Here, we used a CMRxRecon dataset [28] of 100 healthy cases to train all deep learning methods, and then reconstructed a cardiac cine dataset of 5 patients with hypertrophic cardiomyopathy.

Since objective criteria (e.g., RLNE, PSNR, and SSIM) might not comprehensively reflect image quality, we also conducted a reader study online through our CloudBrain platform [45, 46] (<https://csrc.xmu.edu.cn/CloudBrain.html>). Six readers were invited (4 radiologists with 3/8/10/12 years' experience and 2 cardiologists with 10/12 years' experience), to independently evaluate reconstructed images from a diagnostic perspective. They were blind to all reconstruction methods, while fully sampled images were provided for reference. Three clinical-concerned criteria including signal-to-noise ratio (SNR), artifacts suppression, and overall image quality were used. Using a 5-point scale, each criterion ranged from 0 to 5 with a precision of 0.1 (i.e., 0~1: Non-diagnostic; 1~2: Poor; 2~3: Adequate; 3~4: Good; 4~5: Excellent).

Table I shows that the proposed DeepSSL obtains highest mean scores and is the only one which all three criteria of reader study are higher or very close to 4, indicating its image quality basically steps into an excellent level from a diagnostic

perspective. Besides, the differences between DeepSSL and other compared methods are statistically significant according to all p-values of the Wilcoxon signed rank test  $< 0.001$ . As for other compared methods, they have some artifacts in the reconstructed images (Marked with white arrows in Fig. 9), resulting in lower scores that can only reach the adequate or good level. These results are consistent with the superiority of DeepSSL on the objective criteria (RLNE, PSNR, and SSIM) in Table II.

TABLE I  
THE SCORES OF THE READER STUDY [MEAN±STD].

Data	Method	SNR	Artifacts suppression	Overall image quality
SAX view	L+S	3.10±0.31	3.04±0.48	3.29±0.45
	DL-ESPIRiT	3.60±0.31	3.43±0.36	3.62±0.34
	SLR-Net	4.05±0.28	3.74±0.37	3.99±0.36
	DeepSSL	<b>4.23±0.24</b>	<b>3.98±0.26</b>	<b>4.21±0.25</b>
LAX view	L+S	2.87±0.30	2.99±0.51	3.01±0.36
	DL-ESPIRiT	3.61±0.46	3.39±0.60	3.54±0.48
	SLR-Net	3.93±0.38	3.65±0.56	3.88±0.35
	DeepSSL	<b>4.17±0.35</b>	<b>3.94±0.56</b>	<b>4.16±0.33</b>

Note: There are 120 SAX images and 120 LAX images from 5 patients used for the reader study. The means and standard deviations are computed over all images, respectively. The highest scores are bold faced. All compared methods are statistically significant difference ( $p < 0.001$ ) compared to our DeepSSL under Wilcoxon signed-rank test.

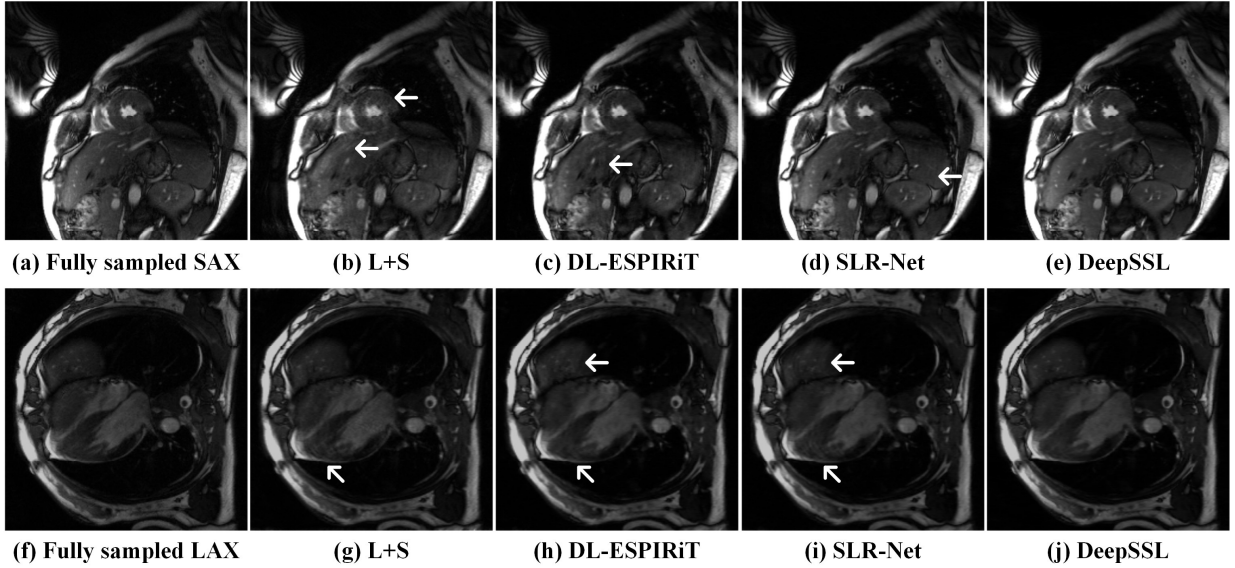


Fig. 9. Reconstruction results of a cardiac cine patient dataset of SAX and LAX views using different methods. (a) (or (f)) is the fully sampled image. (b)-(e) (or (g)-(j)) are reconstructed images. Note: The k-t random undersampling pattern with AF=6 is used. Obvious artifacts are marked with white arrows.

TABLE II

RLNE ( $\times 10^{-2}$ )/PSNR (dB)/SSIM ( $\times 10^{-2}$ ) OF PATIENT RECONSTRUCTIONS UNDER K-T RANDOM UNDERSAMPLING PATTERN WITH AF=6 [MEAN $\pm$ STD].

Data	Method	RLNE	PSNR	SSIM
SAX view	L+S	10.66 $\pm$ 3.80	38.89 $\pm$ 2.76	94.92 $\pm$ 2.43
	DL-ESPIRiT	8.53 $\pm$ 1.99	40.61 $\pm$ 2.18	95.32 $\pm$ 1.69
	SLR-Net	8.47 $\pm$ 2.04	40.68 $\pm$ 2.21	95.07 $\pm$ 1.72
	DeepSSL	<b>7.74<math>\pm</math>1.43</b>	<b>41.38<math>\pm</math>1.99</b>	<b>95.55<math>\pm</math>1.45</b>
LAX view	L+S	13.59 $\pm$ 4.32	36.62 $\pm$ 2.29	93.92 $\pm$ 1.98
	DL-ESPIRiT	10.59 $\pm$ 2.41	38.61 $\pm$ 1.67	94.83 $\pm$ 1.56
	SLR-Net	10.09 $\pm$ 2.49	39.07 $\pm$ 1.97	94.91 $\pm$ 1.54
	DeepSSL	<b>9.38<math>\pm</math>1.56</b>	<b>39.60<math>\pm</math>1.86</b>	<b>95.05<math>\pm</math>1.67</b>

Note: The means and standard deviations are computed over all test data, respectively. The lowest RLNE, highest PSNR and SSIM values are bold faced.

These results demonstrate that, from both objective and clinical-concerned subjective criteria, our technique is adaptive to cardiac patients and provides reliable image reconstructions.

## IV. DISCUSSIONS

### A. Example Downstream Task: Cardiac Segmentation

Generally, high-quality reconstructions benefit downstream tasks in image analysis, achieving close performance compared to fully sampled images. Here, we focused on the downstream task of cardiac segmentation, which played a crucial role in clinical diagnosis and analysis.

We first trained a state-of-the-art cardiac segmentation network [47] using a public CMRxRecon dataset with manual segmentation ground truth [28]. Then, this network was used to compare the performance of reconstructed images using different methods for SAX cardiac segmentation. To quantify the segmentation accuracy, the Dice coefficient was utilized. A higher Dice coefficient indicates the better segmentation.

Table III and Fig. 10 show that the segmentation results of our DeepSSL are more accurate than other methods, indicated by better smoothness and continuity in shape, as well as higher Dice coefficients. Meanwhile, DeepSSL's results are closest to

the fully sampled ones. Segmentation results of other four methods are good in the left ventricle and myocardium, but there are significant loss in the right ventricle (Figs. 10(c)-(e)).

TABLE III

DICE COEFFICIENT ( $\times 10^{-2}$ ) IN THE CARDIAC SEGMENTATION [MEAN $\pm$ STD].

Method	LV	MYO	RV	Average
Fully sampled	<b>94.93<math>\pm</math>2.71</b>	<b>84.93<math>\pm</math>3.95</b>	<b>93.92<math>\pm</math>3.22</b>	<b>91.26<math>\pm</math>4.49</b>
DCCNN	94.30 $\pm$ 2.75	82.46 $\pm$ 4.79	92.87 $\pm$ 3.22	89.88 $\pm$ 5.28
DL-ESPIRiT	94.42 $\pm$ 2.73	82.72 $\pm$ 4.59	92.49 $\pm$ 3.22	89.88 $\pm$ 5.12
SLR-Net	94.23 $\pm$ 2.61	82.54 $\pm$ 4.63	92.70 $\pm$ 3.23	89.83 $\pm$ 5.19
DeepSSL	<b>94.55<math>\pm</math>2.63</b>	<b>83.34<math>\pm</math>4.49</b>	<b>93.41<math>\pm</math>3.22</b>	<b>90.43<math>\pm</math>5.04</b>

Note: Images for segmentation are reconstructed using different methods under the k-t random undersampling pattern with AF=6. The means and standard deviations are computed over all images, respectively. "LV", "MYO", "RV" denote left ventricle, myocardium, and right ventricle, respectively. "Average" denotes averaging the values of the three Dice coefficients. The Dice coefficients of fully sampled and closest to fully sampled are bold faced.

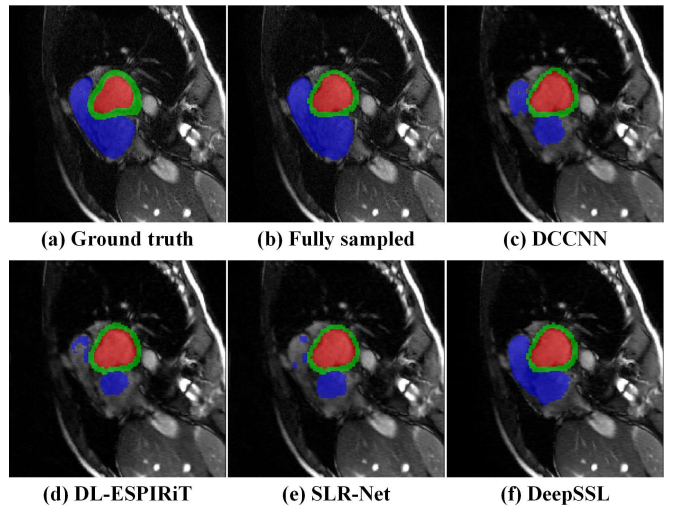


Fig. 10. Cardiac segmentation results of different methods. (a) is the ground truth. (b) is segmented using fully sampled image. (c)-(f) are segmented using reconstructed images from different methods. Note: The k-t random undersampling pattern with AF=6 is used.



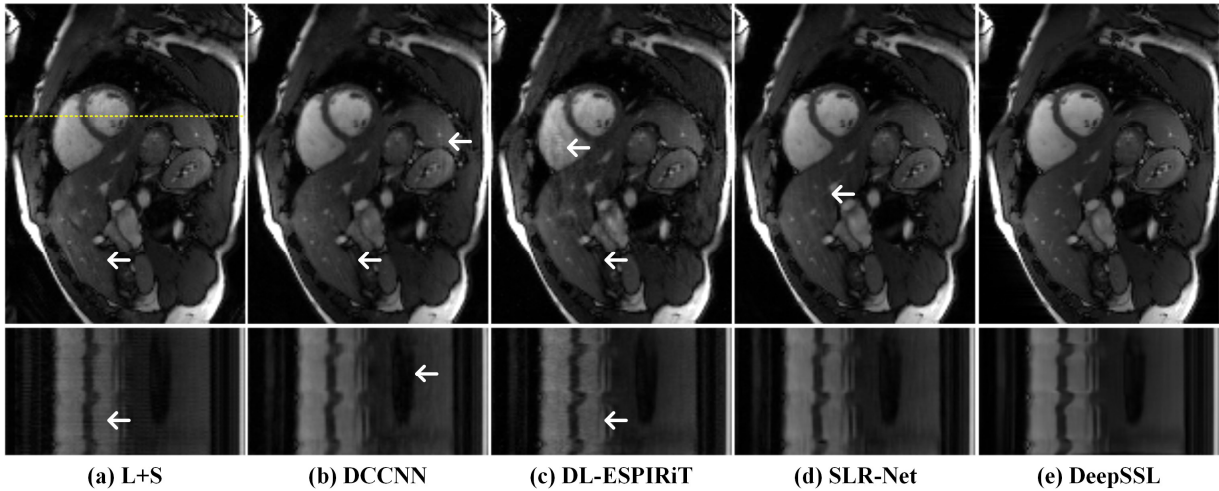


Fig. 11. Prospective reconstruction results of a real-time cardiac cine dataset using different methods. (a)-(e) are reconstructed images. Note: The k-t VISTA pattern with AF=8 is used. The 2D spatiotemporal images are given for each reconstruction and their corresponding extracted position is marked by the yellow dotted line. Obvious artifacts are marked with white arrows.

### B. Prospective Study: Real-Time Cardiac Cine MRI

In addition to the aforementioned retrospective studies, we further explored the robustness of the proposed method to the prospective imaging experiment.

A free-breathing undersampled cardiac cine data from the public OCMR dataset [27] was used. It has 3 SAX slices of size  $320 \times 120$  with 65 temporal frames and is prospectively undersampled using a k-t VISTA pattern with AF=8. In this experiment, all deep learning methods were trained under k-t VISTA undersampling with AF=8 but used a same dataset as before.

Fig. 11 shows that the proposed DeepSSL is superior to other compared methods in terms of artifacts suppression and details preservation, and captures the organ motion precisely. L+S, DCCNN, and DL-ESPIRiT still exhibit obvious streaking artifacts (Marked with white arrows) and spatial blurring. SLR-Net provides nice dynamic information, but spatial artifacts remain slightly.

## V. CONCLUSION

Our work presents a novel dimension-reduced separable learning scheme, integrated with spatiotemporal priors, culminating in the development of a Deep Separable Spatiotemporal Learning network (DeepSSL) tailored for dynamic cardiac magnetic resonance imaging (MRI). This network unrolls an iteration process of a reconstruction model with both temporal low-rankness and spatial sparsity, demonstrating efficiency even with highly limited training data (e.g., only 5 cases). Besides, the network behavior is preliminarily revealed by visualizing its intermediate outputs.

Extensive evaluations on *in vivo* datasets showcase that for both healthy cases and patients, the proposed DeepSSL achieves state-of-the-art performance, both visually and quantitatively, while reducing the demand for training cases by up to 75% (i.e., 25 cases achieved). The reliability of DeepSSL in the diagnostic perspective is further affirmed through validation by four experienced radiologists and two

cardiologists. Additionally, our method proves beneficial for the downstream task of cardiac segmentation and exhibits robustness in prospective real-time cardiac MRI reconstruction.

Our study demonstrates that separable deep learning effectively mitigates problem dimensions, reduces the reliance on training data volume, and lessens the computing device requirements. This innovative approach holds promise in addressing the escalating demand for high-dimensional data reconstruction in MRI applications.

## ACKNOWLEDGMENTS

The authors thank Drs. Michael Lustig, Ricardo Otazo, Jo Schlemper, Christopher M. Sandino, Dong Liang, and Yongchao Xu for sharing their codes online.

## REFERENCES

- [1] P. J. Keall *et al.*, “Integrated MRI-guided radiotherapy — Opportunities and challenges,” *Nat. Rev. Clin. Oncol.*, vol. 19, no. 7, pp. 458-470, 2022.
- [2] M. Lustig, D. Donoho, and J. M. Pauly, “Sparse MRI: The application of compressed sensing for rapid MR imaging,” *Magn. Reson. Med.*, vol. 58, no. 6, pp. 1182-1195, 2007.
- [3] K. P. Pruessmann, M. Weiger, M. B. Scheidegger, and P. Boesiger, “SENSE: Sensitivity encoding for fast MRI,” *Magn. Reson. Med.*, vol. 42, no. 5, pp. 952-962, 1999.
- [4] M. A. Griswold *et al.*, “Generalized autocalibrating partially parallel acquisitions (GRAPPA),” *Magn. Reson. Med.*, vol. 47, no. 6, pp. 1202-1210, 2002.
- [5] Z. Liang, “Spatiotemporal imaging with partially separable functions,” in *4th IEEE International Symposium on Biomedical Imaging (ISBI)*, 2007, pp. 988-991.
- [6] R. Otazo, D. Kim, L. Axel, and D. K. Sodickson, “Combination of compressed sensing and parallel imaging for highly accelerated first-pass cardiac perfusion MRI,” *Mag. Reson. Med.*, vol. 64, no. 3, pp. 767-776, 2010.
- [7] M. Usman, C. Prieto, T. Schaeffter, and P. G. Batchelor, “k-t group sparse: A method for accelerating dynamic MRI,” *Mag. Reson. Med.*, vol. 66, no. 4, pp. 1163-1176, 2011.
- [8] L. Feng *et al.*, “Highly accelerated real-time cardiac cine MRI using k-t SPARSE-SENSE,” *Magn. Reson. Med.*, vol. 70, no. 1, pp. 64-74, 2013.
- [9] J. Caballero, A. N. Price, D. Rueckert, and J. V. Hajnal, “Dictionary learning and time sparsity for dynamic MR data reconstruction,” *IEEE Trans. Med. Imaging*, vol. 33, no. 4, pp. 979-994, 2014.

- [10] Y. Hu *et al.*, "Spatiotemporal flexible sparse reconstruction for rapid dynamic contrast-enhanced MRI," *IEEE Trans. Biomed. Eng.*, vol. 69, no. 1, pp. 229-243, 2022.
- [11] S. G. Lingala, Y. Hu, E. DiBella, and M. Jacob, "Accelerated dynamic MRI exploiting sparsity and low-rank structure: k-t SLR," *IEEE Trans. Med. Imaging*, vol. 30, no. 5, pp. 1042-1054, 2011.
- [12] K. H. Jin, D. Lee, and J. C. Ye, "A general framework for compressed sensing and parallel MRI using annihilating filter based low-rank Hankel matrix," *IEEE Trans. Comput. Imaging*, vol. 2, no. 4, pp. 480-495, 2016.
- [13] M. Jacob, M. P. Mani, and J. C. Ye, "Structured low-rank algorithms: Theory, magnetic resonance applications, and links to machine learning," *IEEE Signal Process. Mag.*, vol. 37, no. 1, pp. 54-68, 2020.
- [14] X. Zhang *et al.*, "Accelerated MRI reconstruction with separable and enhanced low-rank Hankel regularization," *IEEE Trans. Med. Imaging*, vol. 41, no. 9, pp. 2486-2498, 2022.
- [15] B. Zhao, J. P. Haldar, A. G. Christodoulou, and Z. Liang, "Image reconstruction from highly undersampled (k,t)-space data with joint partial separability and sparsity constraints," *IEEE Trans. Med. Imaging*, vol. 31, no. 9, pp. 1809-1820, 2012.
- [16] R. Otazo, E. Candès, and D. K. Sodickson, "Low-rank plus sparse matrix decomposition for accelerated dynamic MRI with separation of background and dynamic components," *Magn. Reson. Med.*, vol. 73, no. 3, pp. 1125-1136, 2015.
- [17] S. Wang *et al.*, "Accelerating magnetic resonance imaging via deep learning," in *IEEE 13th International Symposium on Biomedical Imaging (ISBI)*, 2016, pp. 514-517.
- [18] Y. Yang, J. Sun, H. Li, and Z. Xu, "ADMM-CSNet: A deep learning approach for image compressive sensing," *IEEE Trans. Pattern Anal. Mach. Intell.*, vol. 42, no. 3, pp. 521-538, 2020.
- [19] E. J. Zucker, C. M. Sandino, A. Kino, P. Lai, and S. S. Vasanawala, "Free-breathing accelerated cardiac MRI using deep learning: Validation in children and young adults," *Radiology*, vol. 300, no. 3, pp. 539-548, 2021.
- [20] Q. Yang, Z. Wang, K. Guo, C. Cai, and X. Qu, "Physics-driven synthetic data learning for biomedical magnetic resonance: The imaging physics-based data synthesis paradigm for artificial intelligence," *IEEE Signal Process. Mag.*, vol. 40, no. 2, pp. 129-140, 2023.
- [21] A. Kofler, M. Dewey, T. Schaeffter, C. Wald, and C. Kolbitsch, "Spatio-temporal deep learning-based undersampling artefact reduction for 2D radial cine MRI with limited training data," *IEEE Trans. Med. Imaging*, vol. 39, no. 3, pp. 703-717, 2020.
- [22] A. Hauptmann, S. Arridge, F. Lucka, V. Muthurangu, and J. A. Steeden, "Real-time cardiovascular MR with spatio-temporal artifact suppression using deep learning-proof of concept in congenital heart disease," *Magn. Reson. Med.*, vol. 81, no. 2, pp. 1143-1156, 2019.
- [23] J. Schlemper, J. Caballero, J. V. Hajnal, A. N. Price, and D. Rueckert, "A deep cascade of convolutional neural networks for dynamic MR image reconstruction," *IEEE Trans. Med. Imaging*, vol. 37, no. 2, pp. 491-503, 2018.
- [24] C. M. Sandino, P. Lai, S. S. Vasanawala, and J. Y. Cheng, "Accelerating cardiac cine MRI using a deep learning-based ESPIRiT reconstruction," *Magn. Reson. Med.*, vol. 85, no. 1, pp. 152-167, 2021.
- [25] Z. Ke *et al.*, "Learned low-rank priors in dynamic MR imaging," *IEEE Trans. Med. Imaging*, vol. 40, no. 12, pp. 3698-3710, 2021.
- [26] W. Huang *et al.*, "Deep low-rank plus sparse network for dynamic MR imaging," *Med. Image Anal.*, vol. 73, p. 102190, 2021.
- [27] C. Chen *et al.*, "OCMR (v1.0)—Open-access multi-coil k-space dataset for cardiovascular magnetic resonance imaging," arXiv: 2008.03410, 2020.
- [28] C. Wang *et al.*, "CMRxRecon: An open cardiac MRI dataset for the competition of accelerated image reconstruction," arXiv: 2309.10836, 2023.
- [29] Z. Wang *et al.*, "One-dimensional deep low-rank and sparse network for accelerated MRI," *IEEE Trans. Med. Imaging*, vol. 42, no. 1, pp. 79-90, 2023.
- [30] Z. Wang *et al.*, "One for multiple: Physics-informed synthetic data boosts generalizable deep learning for fast MRI reconstruction," arXiv: 2307.13220, 2023.
- [31] R. Ahmad, H. Xue, S. Giri, Y. Ding, J. Craft, and O. P. Simonetti, "Variable density incoherent spatiotemporal acquisition (VISTA) for highly accelerated cardiac MRI," *Magn. Reson. Med.*, vol. 74, no. 5, pp. 1266-1278, 2015.
- [32] Y. Yang, F. Liu, Z. Jin, and S. Crozier, "Aliasing artefact suppression in compressed sensing MRI for random phase-encode undersampling," *IEEE Trans. Biomed. Eng.*, vol. 62, no. 9, pp. 2215-2223, 2015.
- [33] Y. Liu, Z. Zhan, J.-F. Cai, D. Guo, Z. Chen, and X. Qu, "Projected iterative soft-thresholding algorithm for tight frames in compressed sensing magnetic resonance imaging," *IEEE Trans. Med. Imaging*, vol. 35, no. 9, pp. 2130-2140, 2016.
- [34] X. Zhang *et al.*, "A guaranteed convergence analysis for the projected fast iterative soft-thresholding algorithm in parallel MRI," *Med. Image Anal.*, vol. 69, p. 101987, 2021.
- [35] M. V. Afonso, J. M. Bioucas-Dias, and M. A. T. Figueiredo, "Fast image recovery using variable splitting and constrained optimization," *IEEE Trans. Image Process.*, vol. 19, no. 9, pp. 2345-2356, 2010.
- [36] D. Liang, J. Cheng, Z. Ke, and L. Ying, "Deep magnetic resonance image reconstruction: Inverse problems meet neural networks," *IEEE Signal Process. Mag.*, vol. 37, no. 1, pp. 141-151, 2020.
- [37] A. Pramanik, H. Aggarwal, and M. Jacob, "Deep generalization of structured low-rank algorithms (Deep-SLR)," *IEEE Trans. Med. Imaging*, vol. 39, no. 12, pp. 4186-4197, 2020.
- [38] K. He, X. Zhang, S. Ren, and J. Sun, "Deep residual learning for image recognition," in *IEEE Conference on Computer Vision and Pattern Recognition (CVPR)*, 2016, pp. 770-778.
- [39] J. Zhang and B. Ghanem, "ISTA-Net: Interpretable optimization-inspired deep network for image compressive sensing," in *IEEE Conference on Computer Vision and Pattern Recognition (CVPR)*, 2018, pp. 1828-1837.
- [40] Z. Wang *et al.*, "A sparse model-inspired deep thresholding network for exponential signal reconstruction—Application in fast biological spectroscopy," *IEEE Trans. Neural Netw. Learn. Syst.*, vol. 34, no. 10, pp. 7578-7592, 2023.
- [41] D. Kingma and J. Ba, "Adam: A method for stochastic optimization," arXiv: 1603.04467, 2014.
- [42] M. Uecker *et al.*, "ESPIRiT—An eigenvalue approach to autocalibrating parallel MRI: Where SENSE meets GRAPPA," *Magn. Reson. Med.*, vol. 71, no. 3, pp. 990-1001, 2014.
- [43] X. Qu, Y. Hou, F. Lam, D. Guo, J. Zhong, and Z. Chen, "Magnetic resonance image reconstruction from undersampled measurements using a patch-based nonlocal operator," *Med. Image Anal.*, vol. 18, no. 6, pp. 843-856, 2014.
- [44] W. Zhou, A. C. Bovik, H. R. Sheikh, and E. P. Simoncelli, "Image quality assessment: From error visibility to structural similarity," *IEEE Trans. Image Process.*, vol. 13, no. 4, pp. 600-612, 2004.
- [45] Y. Zhou *et al.*, "XCloud-pFISTA: A medical intelligence cloud for accelerated MRI," in *43rd Annual International Conference of the IEEE Engineering in Medicine and Biology Society (EMBC)*, 2021, pp. 3289-3292.
- [46] Y. Zhou *et al.*, "CloudBrain-ReconAI: An online platform for MRI reconstruction and image quality evaluation," arXiv: 2212.01878, 2022.
- [47] F. Cheng *et al.*, "Learning directional feature maps for cardiac MRI segmentation," in *Medical Image Computing and Computer Assisted Intervention (MICCAI)*, 2020, pp. 108-117.